

Article

Improved Linear Active Disturbance Rejection Control for IPMSM Drives Considering Load Inertia Mismatch

Feng Jiang , Fan Yang , Songjun Sun and Kai Yang *

State Key Laboratory of Advanced Electromagnetic Engineering and Technology, School of Electrical and Electronic Engineering, Huazhong University of Science and Technology, Wuhan 430074, China; jiangfeng@hust.edu.cn (F.J.); fang_yang@hust.edu.cn (F.Y.); songjunsun@foxmail.com (S.S.)

* Correspondence: yk@mail.hust.edu.cn

Abstract: This article presents an improved linear active disturbance rejection control (LADRC) method for interior permanent magnet synchronous motor (IPMSM) drives. The proposed method adopts a dual LADRC structure. The outer LADRC-based speed regulator adopts position feedback instead of speed feedback so that the low-pass filter for speed calculation can be eliminated. The inner LADRC-based current regulator incorporates a maximum torque per ampere (MTPA) operation scheme to improve the torque output capacity and the efficiency of the motor. In addition, considering the variation of load inertia in real applications, a systematic modelling and analysis on the effect of inertia mismatch is presented. To enhance the robustness of the drive system to inertia mismatch, an inertia identification method is proposed, in which the inertia information is extracted from the estimated disturbance of speed loop LESO. Finally, the effectiveness of the proposed method is verified on a 1.0-kW IPMSM drive platform.

Keywords: interior permanent magnet synchronous motor (IPMSM); linear active disturbance rejection control (LADRC); speed regulation; inertia identification



Citation: Jiang, F.; Yang, F.; Sun, S.; Yang, K. Improved Linear Active Disturbance Rejection Control for IPMSM Drives Considering Load Inertia Mismatch. *Energies* **2022**, *15*, 1169. <https://doi.org/10.3390/en15031169>

Academic Editors: Baoling Guo, Hebertt Sira Ramirez and Rafal Madonski

Received: 25 December 2021

Accepted: 2 February 2022

Published: 5 February 2022

Publisher's Note: MDPI stays neutral with regard to jurisdictional claims in published maps and institutional affiliations.



Copyright: © 2022 by the authors. Licensee MDPI, Basel, Switzerland. This article is an open access article distributed under the terms and conditions of the Creative Commons Attribution (CC BY) license (<https://creativecommons.org/licenses/by/4.0/>).

1. Introduction

Interior permanent magnet synchronous motors (IPMSMs) are increasingly used in household and industrial applications due to their advantages of simple structure, high-torque density, low cost, and good dynamic response [1]. To guarantee a good driving performance, the output speed of the motor should not only be able to track the reference speed accurately and promptly, but also recover to steady state quickly under the influence of disturbance. The typical field-oriented control (FOC) topology for IPMSM is designed to be a double-loop structure, where the outer speed loop is in cascade with the inner current loop. Then, the speed and the current can both be controlled through closed-loop regulation. For this control topology, the speed and current regulators play a key role in the performance of the whole IPMSM drive system.

The proportional-integral (PI) control, owing to the advantage of relatively simple structure, high stability, and low steady-state error, is already widely applied in speed and current regulation of IPMSM drives [2]. However, the IPMSM drive system is a typical nonlinear system. The internal model parameter variations resulting from crossing coupling, magnetic saturation, temperature change, and especially the load inertia change, will induce time-varying and nonlinear characteristics to the model. In this case, the PI control scheme cannot achieve a satisfying dynamic performance in the entire operation range [3]. To this end, substantial efforts have been devoted to developing nonlinear control schemes, such as sliding mode control [4,5], predictive control [6], robustness control [7], backstepping control [8], and artificial intelligence-based control [9].

The abovementioned control schemes possess their own advantages in handling nonlinear plants. Nevertheless, the various disturbances in the IPMSM drive system still bring

challenges for controllers to achieve better performance. In practical applications, IPMSM drive systems are inevitably confronted with various unmeasured disturbances, which may come internally, such as unmodelled dynamics and parameter mismatches, or externally, such as load disturbance. However, the abovementioned schemes are all feedback-based schemes, which means they can only generate the control command through feedback regulation, rather than react directly and promptly to attenuate these disturbances. Although these schemes can finally eliminate the adverse influence of disturbances, it is in a relatively slow way, resulting in the degradation of dynamic performance.

An efficient way to enhance the robustness of the drive system against disturbances and to further exploit the fast dynamic capacities of IPMSM is to introduce an additional feedforward path into the controller besides the traditional feedback path. The newly formulated controller is also known as the two-degree-of-freedom controller [10], which can counteract the influence of disturbances by using the estimated disturbances to compensate for them in the feedforward path. Among those two-degree-of-freedom methods, active disturbance rejection control (ADRC) shows great prospects due to its unique advantages in handling systems with various uncertainties and disturbance [11]. The original ADRC is a nonlinear structure with a nonlinear state feedback function, which is designed to achieve a higher convergence rate [12]. However, this leads to the algorithm being difficult to implement, and makes the stability analysis rather complicated. To this end, Gao simplified this method into a linear version with linear state feedback, known as LADRC [13]. For the LADRC, the issue of parameter tuning is reduced to the adjustment of bandwidth. Moreover, since the controller is linearized, the conventional frequency-domain method can be adopted to analyze the stability of the controller, which facilitates its application.

In recent years, LADRC has been widely applied in motor drive systems. The LADRC-based regulator can be utilized for current control [14], speed control [15–18], or both [11,19,20]. In [20], a dual LADRC-based control scheme is proposed, in which the speed LADRC considers the disturbance induced from iron losses, and the current LADRC minimizes the torque ripple by estimating the disturbance corresponding to the back-EMF. In [21], a higher-order LADRC is studied, in which the conventional dual loop structure is replaced by a single loop structure. Thus, the speed can be directly controlled with faster dynamics. The successful application of LADRC further stimulates the theoretical analysis to go deeper. In [18], the theoretical comparisons among the PI controller, the disturbance observer (DOB)-based controller, and the LADRC are conducted to show the superiority of LADRC. In [22], a frequency-domain interpretation of the second-order LADRC is proposed to reveal the association between the LADRC and the PID. In [23], the relationship between the high-order LADRC and the cascaded low-order LADRCs are explored.

Numerous applications have proved the effectiveness of LADRC in motor control systems. However, for speed control in practical IPMSM drives, there are still some problems that have not yet been fully investigated. Firstly, to achieve closed-loop speed control, the feedback information of rotational speed should be obtained. However, in most application scenarios, the motion sensors mounted on the shaft of the motor are position sensors, such as Hall sensors, optical encoders, or resolvers. Therefore, a low-pass filter is mandatory for suppressing the noise in the process of extracting speed information from the position. Secondly, the rotor magnetic saliency of IPMSM increases the q -axis inductance and results in a reluctance torque in addition to the permanent magnet torque [24]. In this case, an MTPA operation scheme is usually adopted to exploit the torque output capability [1,25,26]. Therefore, it would be necessary to improve the conventional LADRC method so as to achieve MTPA operation. Thirdly, to guarantee high performance control of speed, the inertia information of the IPMSM drive system is required. However, in some applications, such as CNC machine tools or winding machines, the inertia may be time-varying. Even though the LADRC can deal with such uncertainties by estimating and compensating for them using linear extended state observer (LESO), it does not mean that the overall performance of the system remains intact. In fact, the kernel of LADRC's disturbance rejection capability lies in timely and accurate estimation of disturbance. Any

mismatch between the actual inertia and the modeled inertia will be regarded as internal disturbance, thereby increasing the estimation burden of LESO, and further degrading the system performance. In [18], the influence of inertia mismatch on the performance of a surface-mounted PMSM (SPMSM) drive system is discussed. However, the influence of low-pass filter for feedback speed calculation is ignored.

Therefore, to deal with the above mentioned three problems, this article proposes an improved LADRC-based controller for IPMSM drives. The main contributions of this article are summarized as follows.

- (1) Considering that the typical motion sensor of the IPMSM drive is a position sensor, a third-order LADRC for speed regulation is proposed, in which the position is used as the feedback state. Thus, the low-pass filter for speed calculation can be eliminated.
- (2) To fully exploit the torque output capability of the IPMSM, the MTPA operation scheme is incorporated into the proposed LADRC-based method.
- (3) The effect of load inertia mismatch to the system stability, the tracking performance, and the disturbance rejection property is systematically analyzed. To enhance the robustness of the system to inertia mismatch, an inertia identification method is proposed.
- (4) The proposed LADRC-based method and the load inertia identification method are verified by experimental study.

The remainder of this article are organized as follows. Section 2 gives a brief description of the dynamic IPMSM model. Section 3 introduces the design of the LADRC-based speed and current regulators. Section 4 analyzes the influence of inertia mismatch on the performance of the LADRC-based drive system. Section 5 presents an improved LADRC-based speed regulator with inertia identification. Finally, the experimental results are shown in Section 6, and the conclusions are drawn in Section 7.

2. Dynamic Model of IPMSM

To simplify the modeling of IPMSM, it is commonly assumed that the employed IPMSM has negligible magnetic saturation, cross-coupling, iron losses, and eddy current losses. Moreover, the three-phase windings are symmetric, and the magnetic field in the airgap is sinusoidal. Thus, the stator current dynamics of IPMSM can be described in the d - q synchronous reference frame as:

$$\begin{cases} \dot{i}_d = -\frac{R_s}{L_d}i_d + \frac{1}{L_d}u_d + n_p\omega_r\frac{L_q}{L_d}i_q \\ \dot{i}_q = -\frac{R_s}{L_q}i_q + \frac{1}{L_q}u_q - n_p\omega_r\frac{L_d i_d + \psi_f}{L_q} \end{cases} \quad (1)$$

and the mechanical motion dynamics is described as:

$$\dot{\omega}_r = \frac{1}{J}T_e - \frac{1}{J}T_L - \frac{B}{J}\omega_r \quad (2)$$

where i_d and i_q are the d - q -axis stator currents; u_d and u_q are the d - q -axis stator voltages; L_d and L_q are the d - q -axis inductances; R_s is the stator winding resistance; ψ_f is the flux linkage of the permanent magnet; n_p is the number of pole pairs; ω_r is the rotor angular velocity (rad/s); B is the viscous friction coefficient (N·m·s/rad); J is the moment of inertia (kg·m²); T_L is the load torque (N·m); and T_e is the electromagnetic torque (N·m). For the employed IPMSM, T_e is expressed as:

$$\begin{aligned} T_e &= \frac{3}{2}n_p[\psi_f + (L_d - L_q)i_d]i_q \\ &= \underbrace{\frac{3}{2}n_p\psi_f i_q}_{T_m} + \underbrace{\frac{3}{2}n_p(L_d - L_q)i_d i_q}_{T_r} \end{aligned} \quad (3)$$

It can be seen in Equation (3) that the electromagnetic torque is comprised of two terms. The first term is the permanent magnet torque T_m . The second term is the reluctance

torque T_r which is proportional to $L_d - L_q$. To fully utilize the reluctance torque, the MTPA operation scheme should be incorporated into the controller.

3. Design of LADRC-Based Speed and Current Regulators with MTPA Scheme

The LADRC-based IPMSM drive system with an MTPA scheme is shown in Figure 1. The overall system is comprised of an IPMSM, a position sensor, a three-phase voltage-source inverter, a SVPWM generator, three coordinate transformation modules, a speed regulator, and two current regulators. Under the field-oriented control topology, the three-phase stator currents are transformed into d -axis and q -axis currents, which respectively represent the flux-producing component and the torque-producing component. The control loop includes a speed loop and two current loops. The speed regulator generates the torque reference, the MTPA scheme generates the d - and q -axis current references according to the torque reference, and the two current regulators generate the d - and q -axis voltage references.

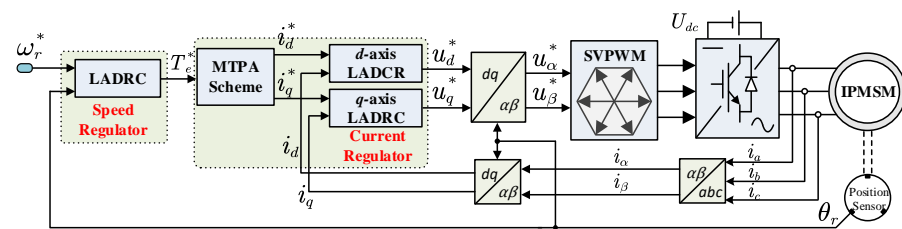


Figure 1. Diagram of the LADRC-based IPMSM drive system with an MTPA scheme.

The speed and current regulators play a key role to the performance of the IPMSM drive system. In this section, a synthesized design for LADRC-based speed and current regulators is presented.

3.1. Design of LADRC-Based Speed Regulator

The key to the application of LADRC is to reformulate the practical controlled plant to a cascaded integral plant and to achieve the modelling of disturbance [11]. To design the speed LADRC, the mechanical motion dynamics of the IPMSM are reformulated as:

$$\begin{cases} \dot{\omega}_r = f_{0n} + f_{1n} + b_n T_e^* \\ f_{0n} = b_n (T_e - T_e^*) - b_n B \hat{\omega}_r \\ f_{1n} = -b_n T_L - b_n B (\omega_r - \hat{\omega}_r) + n_n(t) \end{cases} \quad (4)$$

where T_e^* is the torque reference; b_n is the critical gain and $b_n = 1/J$; f_{0n} and f_{1n} are respectively the known disturbance and the unknown disturbance; the sum of f_{0n} and f_{1n} represents the total disturbance; $\hat{\omega}_r$ is the estimated value of angular velocity; and $n_n(t)$ is the other unknown disturbance, such as unmodeled dynamics and noise.

In Equation (4), the unknown disturbance f_{1n} is distinguished from the known disturbance f_{0n} . It can be seen that f_{1n} consists of the load torque term and the difference term (ω_r and $\hat{\omega}_r$). Therefore, the load torque fluctuation and the sudden speed variation will both be considered in the disturbance model.

Commonly, for the first-order plant presented in Equation (4), a second-order LESO can be designed by regarding f_{1n} as the extended state variable. However, the second-order LESO requires speed feedback information. For most application scenarios, the motion sensors mounted on the shaft of the motor are position sensors, such as Hall sensors, optical encoders, or resolvers. Therefore, the speed information cannot be directly obtained. In order to extract the speed from the measured position, a low-pass filter is required to suppress the noise induced from derivate operation, i.e., $\hat{\omega}_r = \text{LPF}(\dot{\theta}_r)$, where θ_r is the measured rotor position. To eliminate the filter, the second-order plant can be adopted:

$$\begin{cases} \dot{\theta}_r = \omega_r \\ \dot{\omega}_r = f_{0n} + f_{1n} + b_n T_e^* \end{cases} \quad (5)$$

Then, a third-order LESO is designed to estimate the states and the unknown disturbance by using the position feedback instead of speed feedback:

$$\begin{cases} e_{1n} = z_{1n} - \theta_r \\ \dot{z}_{1n} = z_{2n} - \beta_{1n}e_{1n} \\ \dot{z}_{2n} = z_{3n} + f_{0n} + b_n T_e^* - \beta_{2n}e_{1n} \\ \dot{z}_{3n} = -\beta_{3n}e_{1n} \end{cases} \quad (6)$$

where z_{1n}, z_{2n}, z_{3n} are the estimations of $\theta_r, \omega_r, f_{1n}$; e_{1n} is the estimation error of LESO; and $\beta_{1n}, \beta_{2n}, \beta_{3n}$ are the observer gains. For convenience of parameter tuning and theoretical analysis, this article adopts a scaling- and bandwidth-parameterization method [13]. The gains are parameterized as follows:

$$[\beta_{1n} \ \beta_{2n} \ \beta_{3n}] = [3\omega_{0n} \ 3\omega_{0n}^2 \ \omega_{0n}^3] \quad (7)$$

where ω_{0n} is a positive constant denoting the bandwidth of LESO. A higher ω_{0n} helps improve the response rate, but will increase the observer’s sensitivity to noise. In practical applications, ω_{0n} should be designed within reason so as to reach a tradeoff between the rapidity of estimation and the immunity to noise.

The LESO presented in Equation (6) only requires position information θ_r . The rotor speed is estimated through the observer, i.e., $\hat{\omega}_r = z_{2n}$. Therefore, the low-pass filter used for speed calculation is eliminated.

When LESO becomes stable, the estimation error e_{1n} will converge. The speed tracking error of LADRC is defined as $e_s = \omega_r^* - \hat{\omega}_r = \omega_r^* - z_{2n}$. Then, the tracking error dynamic equation can be expressed as:

$$\dot{e}_s = \dot{\omega}_r^* - \dot{z}_{2n} = \dot{\omega}_r^* - (z_{3n} + f_{0n} + b_n T_e^*) \quad (8)$$

By adopting the linear feedback control, the speed tracking error will converge in exponential form:

$$\dot{e}_s = -k_n e_s \quad (9)$$

where k_n is the proportional gain. By substituting Equation (9) into Equation (8), the control law of speed loop LADRC can be derived as:

$$T_e^* = \frac{k_n(\omega_r^* - z_{2n}) + \dot{\omega}_r^* - (z_{3n} + f_{0n})}{b_n} \quad (10)$$

The control law presented in Equation (10) requires the derivative of reference speed as input. This derivative term acts as a feedforward term to track the variation of reference speed, thereby diminishing the oscillation and overshoot during the adjustment of speed. In practical applications, a tracking differentiator (TD) [12] can be adopted to calculate $\dot{\omega}_r^*$. The block diagram of the LADRC-based speed regulator is shown in Figure 2.

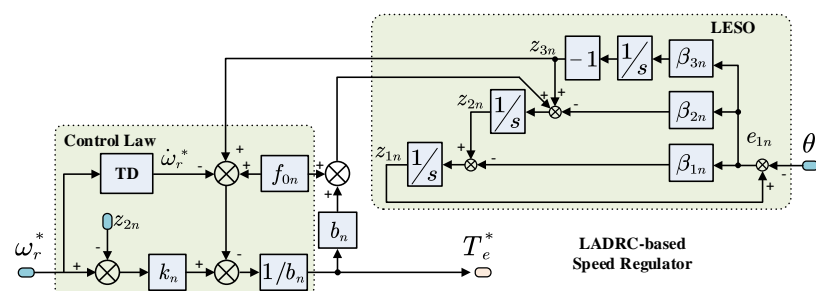


Figure 2. Block diagram of the LADRC-based speed regulator.

3.2. Design of LADRC-Based d - q -Axis Current Regulator with MTPA

3.2.1. d - q -Axis Current Reference Generation Based on MTPA Scheme

The essence of controlling the torque is to control the d - and q -axis currents. In the dual loop control structure, the speed regulator generates the torque reference T_e^* . Therefore, it is necessary to obtain the d - q -axis current reference according to T_e^* . Commonly, the d -axis current reference is set to zero, so that the q -axis current reference will be proportional to T_e^* . However, the rotor magnetic saliency of the IPMSM increases the q -axis inductance and results in a reluctance torque in addition to the permanent magnet torque. To fully exploit the torque output capability of the IPMSM, the maximum torque per ampere (MTPA) operation scheme is adopted. The goal of the MTPA scheme is to achieve the desired torque with a minimum stator current $\sqrt{i_d^2 + i_q^2}$ required, thereby reducing the copper losses and improving the efficiency. The constraints between T_e^* , i_d^* , and i_q^* under MTPA operation is given by:

$$\begin{cases} T_e^* = \frac{3}{2}n_p [\psi_f + (L_d - L_q)i_d^*] \sqrt{\frac{\psi_f i_d^*}{L_d - L_q} + i_d^{*2}} \\ T_e^* = \frac{3}{4}n_p [\psi_f + \sqrt{\psi_f^2 + 4i_q^{*2}(L_d - L_q)^2}] i_q^* \end{cases} \quad (11)$$

The proof for Equation (11) is presented in the Appendix A. For any given torque reference, the d - and q -axis current references required for MPTA operation can be obtained from Equation (11). However, the explicit solution of i_d^* and i_q^* cannot be derived, which makes Equation (11) unsuitable for real-time implementation using microprocessors. To reduce the computation burden, the MTPA scheme can be implemented by means of look-up tables (LUT) with offline calculations [26]. In this article, the LUT method is adopted to achieve MTPA operation.

3.2.2. Current Regulator Design

The current regulator plays a key role in the torque performance of IPMSM. To design the LADRC-based current regulator, the current dynamics of IPMSM are reformulated as:

$$\begin{cases} \dot{i}_d = f_{0d} + f_{1d} + b_d u_d^* \\ f_{0d} = -R_s b_d i_d - n_p \omega_r b_d i_q / b_q \\ f_{1d} = b_d (u_d - u_d^*) + n_d(t) \end{cases} \quad (12)$$

$$\begin{cases} \dot{i}_q = f_{0q} + f_{1q} + b_q u_q^* \\ f_{0q} = -R_s b_q i_q - n_p \omega_r b_q (\psi_f + i_d / b_d) \\ f_{1q} = b_q (u_q - u_q^*) + n_q(t) \end{cases} \quad (13)$$

where u_d^* and u_q^* are the d - q -axis stator voltage references; b_d and b_q are the critical gains, and $b_d = 1/L_d$, $b_q = 1/L_q$; f_{0d} and f_{1d} are respectively the known disturbance and the unknown disturbance of the d -axis; and f_{0q} and f_{1q} are respectively the known disturbance and the unknown disturbance of the q -axis. $n_d(t)$ and $n_q(t)$ are the other unknown disturbance such as unmodeled dynamics and noise.

By regarding the unknown disturbance f_{1d} and f_{1q} as the extended states, the second-order LESOs for d -axis and q -axis are established:

$$\begin{cases} e_{1d} = z_{1d} - i_d \\ \dot{z}_{1d} = z_{2d} + f_{0d} + b_d u_d^* - \beta_{1i} e_{1d} \\ \dot{z}_{2d} = -\beta_{2i} e_{1d} \end{cases} \quad (14)$$

$$\begin{cases} e_{1q} = z_{1q} - i_q \\ \dot{z}_{1q} = z_{2q} + f_{0q} + b_q u_q^* - \beta_{1i} e_{1q} \\ \dot{z}_{2q} = -\beta_{2i} e_{1q} \end{cases} \quad (15)$$

where $z_{1d}, z_{2d}, z_{1q}, z_{2q}$ are the estimations of i_d, f_{1d}, i_q, f_{1q} ; e_{1d}, e_{1q} are the estimation errors of LESO; and β_{1i}, β_{2i} are the observer gains which are parameterized as follows:

$$[\beta_{1i} \ \beta_{2i}] = [2\omega_{0i} \ \omega_{0i}^2] \tag{16}$$

where ω_{0i} is the bandwidth of the current loop LESO.

In analogy with Equation (10), the control law of current loop LADRC can be derived as:

$$u_d^* = \frac{k_d(i_d^* - z_{1d}) + i_d^* - (z_{2d} + f_{0d})}{b_d} \tag{17}$$

$$u_q^* = \frac{k_q(i_q^* - z_{1q}) + i_q^* - (z_{2q} + f_{0q})}{b_q} \tag{18}$$

where k_d and k_q are the proportional gains for the d - and q -axes. The block diagram of the LADRC-based d - q -axis current regulators are shown in Figure 3.

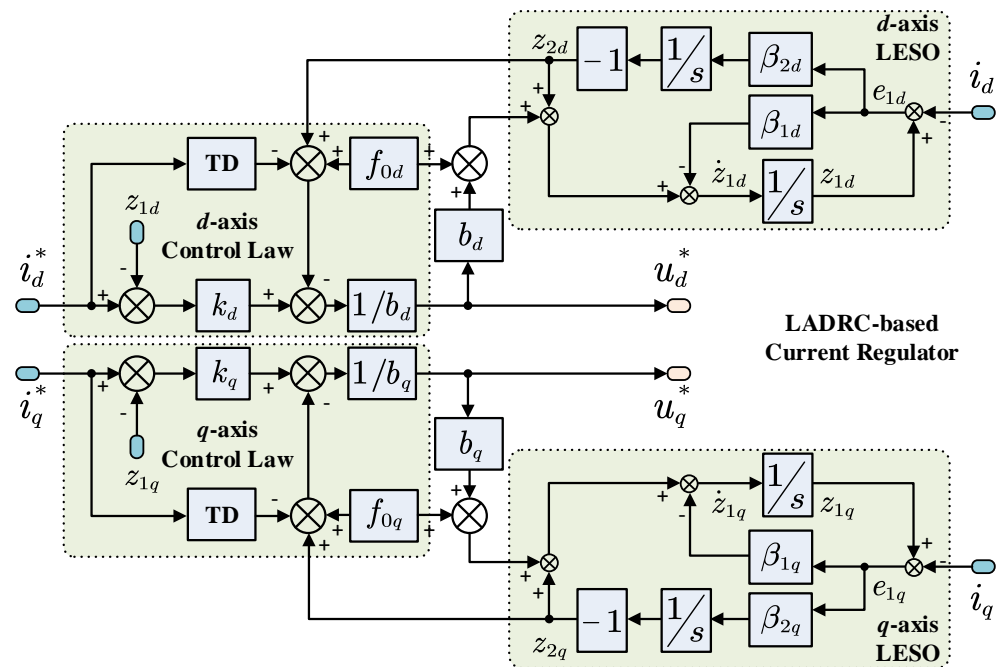


Figure 3. Block diagram of the LADRC-based d - q -axis current regulators.

4. Speed Response of the Drive System in the Presence of Inertia Mismatch

The above designed LADRC-based IPMSM drive system requires information on the machine parameters. In particular, the accuracy of the rotor inertia is highly related to the performance of the speed loop. In some applications, such as CNC machine tools or winding machines, the inertia may be time-varying. Although the LADRC can deal with such uncertainties by estimating and compensating for them by using LESO, this does not mean that the overall performance of the drive system remains intact. In fact, the kernel of LADRC’s disturbance rejection capability lies in timely and accurate estimation of disturbance. Any mismatch between the actual inertia and the modeled inertia will be regarded as internal disturbance, thereby increasing the estimation burden of LESO, and further degrading the system performance. In this section, the speed response of the LADRC-based IPMSM drive system in the presence of inertia mismatch are analyzed in detail.

4.1. Frequency-Domain Derivation of the Speed Response

Considering the inertia mismatch, the LESO and the control law of speed loop LADRC are rewritten as:

$$\begin{cases} e_{1n} = z_{1n} - \theta_r \\ \dot{z}_{1n} = z_{2n} - \beta_{1n}e_{1n} \\ \dot{z}_{2n} = z_{3n} + \hat{f}_{0n} + \hat{b}_n T_e^* - \beta_{2n}e_{1n} \\ \dot{z}_{3n} = -\beta_{3n}e_{1n} \end{cases} \quad (19)$$

$$T_e^* = \frac{k_n(\omega_r^* - z_{2n}) + \dot{\omega}_r^* - (z_{3n} + \hat{f}_{0n})}{\hat{b}_n} \quad (20)$$

where \hat{b}_n and \hat{f}_{0n} are the estimated value of b_n and f_{0n} . Then, by transforming Equation (19) into the frequency-domain, the following transfer functions are obtained:

$$\begin{cases} Z_1(s) = \frac{(\beta_{1n}s^2 + \beta_{2n}s + \beta_{3n})\theta_r(s)}{\lambda(s)} + \frac{s\hat{b}_n T_e^*(s)}{\lambda(s)} + \frac{s\hat{f}_{0n}(s)}{\lambda(s)} \\ Z_2(s) = \frac{s(\beta_{2n}s + \beta_{3n})\theta_r(s)}{\lambda(s)} + \frac{s\hat{b}_n(s + \beta_{1n})T_e^*(s)}{\lambda(s)} + \frac{s(s + \beta_{1n})\hat{f}_{0n}(s)}{\lambda(s)} \\ Z_3(s) = \frac{(\beta_{3n}s^2)\theta_r(s)}{\lambda(s)} - \frac{\hat{b}_n\beta_{3n}T_e^*(s)}{\lambda(s)} - \frac{\beta_{3n}\hat{f}_{0n}(s)}{\lambda(s)} \end{cases} \quad (21)$$

where $\lambda(s)$ is the characteristic polynomial of LESO, $\lambda(s) = s^3 + \beta_{1n}s^2 + \beta_{2n}s + \beta_{3n}$. It should be noted that a lowercase letter is used to represent a time-domain variable, whereas the corresponding capital letter is used to represent the variable in the frequency-domain, e.g., $x(t)$ and $X(s)$.

By transforming Equation (20) into the frequency-domain, and combining it with Equation (21), we obtain:

$$\hat{b}_n T_e^*(s) = \frac{(s + k_n)\lambda(s)}{sG_1(s)}\omega_r^*(s) - \frac{G_2(s)}{sG_1(s)}\omega_r(s) - \hat{f}_{0n}(s) \quad (22)$$

where $G_1(s) = s^2 + (\beta_{1n} + k_n)s + (\beta_{1n}k_n + \beta_{2n})$, $G_2(s) = (\beta_{2n}k_n + \beta_{3n})s + \beta_{3n}k_n$.

Then, transforming Equation (5) into the frequency-domain, and combining it with Equation (22), we obtain:

$$\frac{\hat{b}_n}{b_n} [s\omega_r(s) - F_{0n} - F_{1n}] = \frac{(s + k_n)\lambda(s)}{sG_1(s)}\omega_r^*(s) - \frac{G_2(s)}{sG_1(s)}\omega_r(s) - \hat{f}_{0n}(s) \quad (23)$$

Defining $r_b = \hat{b}_n/b_n$ to denote the mismatch ratio of inertia, Equation (23) is rewritten as:

$$\omega_r(s) = \frac{(s + k_n)\lambda(s)}{R(s)}\omega_r^*(s) + \frac{r_b s G_1(s)}{R(s)}F_{1n}(s) + \frac{s G_1(s)}{R(s)} [r_b F_{0n}(s) - \hat{f}_{0n}(s)] \quad (24)$$

where $R(s)$ is the characteristic polynomial of the closed-loop control system:

$$R(s) = r_b s^4 + (\beta_{1n}r_b + k_n r_b) s^3 + (\beta_{2n}r_b + \beta_{1n}k_n r_b) s^2 + (\beta_{2n}k_n + \beta_{3n}) s + \beta_{3n}k_n \quad (25)$$

Apparently, Equation (24) denotes the speed response with respect to the reference speed and the unknown disturbance in the presence of inertia mismatch. By conducting the frequency-domain analysis, the speed control performance of the LADRC-based drive system can be evaluated.

4.2. Influence of r_b on Closed-Loop Stability

To analyze the influence of r_b on the closed-loop stability of the system, the generalized root locus method is adopted. The main idea of this method is to create a new system which owns the same closed-loop characteristic polynomial as Equation (24), and the open-loop gain of the new system is r_b . Then, by analyzing distribution of the open-loop

zeros and poles of the new system, the closed-loop stability of system Equation (24) can be indirectly investigated.

Firstly, letting the left side and right side of Equation (25) both be divided by $(\beta_3 + \beta_2k_n)s + \beta_3k_n$, and separating r_b from the equation:

$$\frac{R(s)}{(\beta_{3n} + \beta_{2n}k_n)s + \beta_{3n}k_n} = 1 + r_b \frac{s^2 [s^2 + (\beta_{1n} + k_n)s + (\beta_{2n} + \beta_{1n}k_n)]}{(\beta_{3n} + \beta_{2n}k_n)s + \beta_{3n}k_n} \tag{26}$$

Then, the open-loop transfer function of the new system is designed as:

$$G_o(s) = \frac{r_b s^2 [s^2 + (\beta_{1n} + k_n)s + (\beta_{2n} + \beta_{1n}k_n)]}{(\beta_{2n}k_n + \beta_{3n})s + \beta_{3n}k_n} = \frac{r_b s^2 G_1(s)}{G_2(s)} \tag{27}$$

By setting $k_n = 50$, and $\omega_{0n} = 400$ ($\beta_{1n} = 3\omega_{0n}$, $\beta_{2n} = 3\omega_{0n}^2$, $\beta_{3n} = \omega_{0n}^3$) as an example, the root locus plot of Equation (27) with respect to r_b is obtained, as shown in Figure 4.

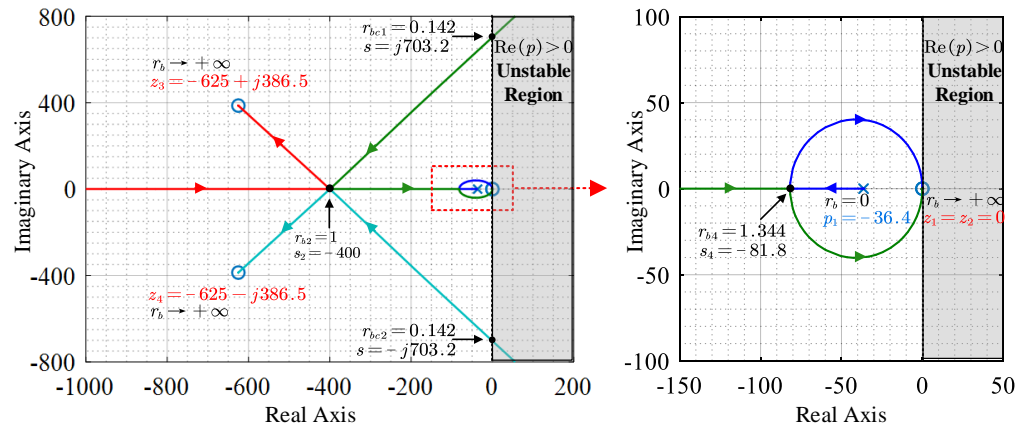


Figure 4. Root locus plot with respect to r_b .

The poles and zeros have been labeled in Figure 4. It can be seen that, if $r_b < 0.142$, a pair of conjugate complex poles are located on the right side of the imaginary axis, which indicates that the system is unstable. To study the influence of r_b on the closed-loop stability in a more specific way, the separation points of the root locus and the intersection points with imaginary axis are derived in the following. Firstly, let:

$$\frac{dG_o(s)}{ds} = 0 \tag{28}$$

The separation points of the root locus and the corresponding r_b are derived:

$$\begin{cases} [s_1 \ s_2 \ s_3 \ s_4] = [0 \ -\omega_{0n} \ -\omega_{0n} \ -\frac{2k_n(k_n + \omega_{0n})}{3k_n + \omega_{0n}}] \\ [r_{b1} \ r_{b2} \ r_{b3} \ r_{b4}] = [\infty \ 1 \ 1 \ \frac{\omega_{0n}^2(\omega_{0n} + 3k_n)^4}{4k_n(\omega_{0n} + k_n)^3(3\omega_{0n}^2 + 6k_n\omega_{0n} - k_n^2)}] \end{cases} \tag{29}$$

Then, let:

$$\text{Re}[1 + G_o(j\omega)] = 0, \text{Im}[1 + G_o(j\omega)] = 0 \tag{30}$$

The intersection points of root locus with the imaginary axis and the corresponding r_b are derived:

$$\begin{cases} \omega_1 = \omega_2 = \pm \sqrt{\frac{\omega_{0n}(3\omega_{0n}^2 + 9k_n\omega_{0n} + 8k_n^2)}{\omega_{0n} + 3k_n}} \\ r_{bc1} = r_{bc2} = \frac{\omega_0(\omega_0 + 3k_n)^2}{(3\omega_{0n} + k_n)(3\omega_{0n}^2 + 9k_n\omega_{0n} + 8k_n^2)} \end{cases} \tag{31}$$

It can be easily proved that $r_{bc1} = r_{bc2} \in (0, 1)$, $r_{b4} \in (1, +\infty)$. Therefore, according to Figure 4 and Equations (29) and (31), the following conclusions can be drawn:

- (1) If $r_b \in (0, r_{bc1})$, a pair of conjugate complex poles are located on the right side of the imaginary axis, thus the system is unstable.
- (2) If $r_b \in (r_{bc1}, 1)$, there exists a pair of conjugate complex poles and a real dominant pole. However, if r_b is very close to r_{bc} , the real part of the complex poles would be very small, and the imaginary part would be very large, thus the overshoot of the system's step response would be very significant.
- (3) If $r_b \in [1, r_{b4}]$, all poles are located on the real axis, thus the step response has no overshoot. Moreover, a larger r_b leads to a faster step response.
- (4) If $r_b \in (r_{b4}, +\infty)$, there exists two pair of conjugate complex poles, the system is always stable in this region, and the overshoot exists but is not significant.

4.3. Influence of r_b on Tracking Performance

According to Equation (24), the transfer function of speed with respect to its reference is described as:

$$G_\omega(s) = \frac{\omega_r(s)}{\omega_r^*(s)} = \frac{(s+k_n)\lambda(s)}{R(s)} \tag{32}$$

$$= \frac{(s+k_n)(s^3+\beta_{1n}s^2+\beta_{2n}s+\beta_{3n})}{r_b s^4 + (\beta_{1n}r_b + k_n r_b) s^3 + (\beta_{2n}r_b + \beta_{1n}k_n r_b) s^2 + (\beta_{2n}k_n + \beta_{3n}) s + \beta_{3n}k_n}$$

Setting $k_n = 50$, and $\omega_{0n} = 400$ ($\beta_{1n} = 3\omega_{0n}^2$, $\beta_{2n} = 3\omega_{0n}$, $\beta_{3n} = \omega_{0n}^3$) as an example, the Bode diagram of the transfer function $G_\omega(s)$ is shown in Figure 5.

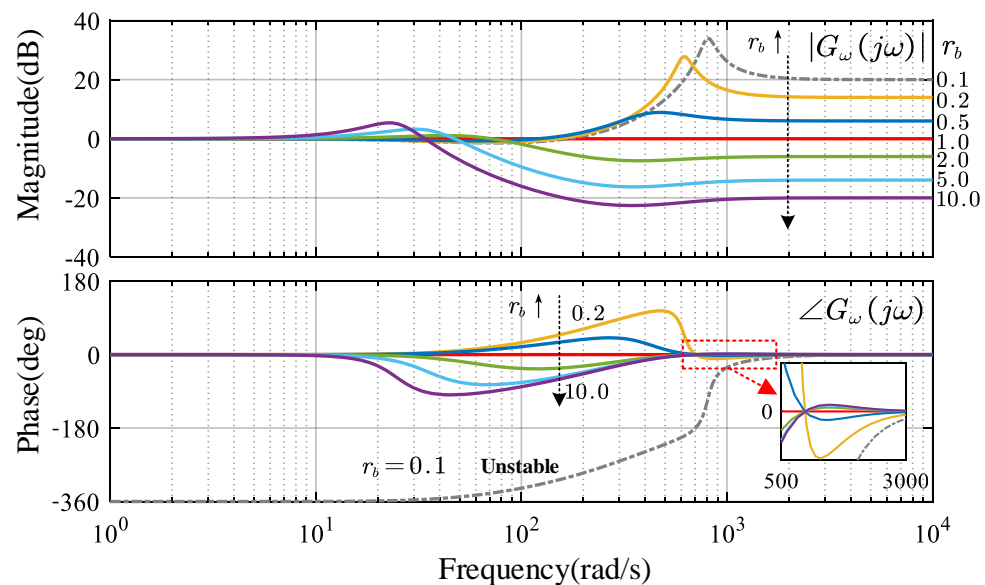


Figure 5. Bode diagram of $G_\omega(s)$ under different r_b .

Figure 5 demonstrates the speed tracking performance of the LADRC-based drive system under different r_b . It can be seen that if $r_b = 1$, the system has the desired speed tracking performance in the whole frequency range. If $r_b \neq 1$, a steady-state tracking error will occur in the medium- and high-frequency range. However, in the low-frequency range, where the reference speed varies slowly, the steady-state tracking error is negligible. Therefore, it is concluded that the tracking performance of the LADRC-based drive system against inertia mismatch decreases as the frequency of the reference increases.

Figure 6 shows the step response of the transfer function $G_\omega(s)$ under different r_b . It can be noted that the system will not achieve the desired response as long as $r_b \neq 1$. If r_b is too small, the step response will diverge, hence the system will be unstable. These results are in accordance with the above frequency analysis.

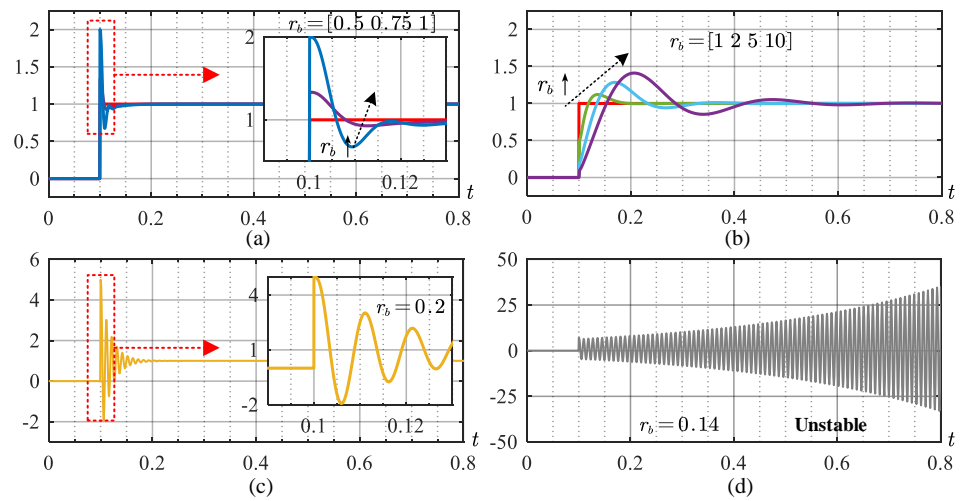


Figure 6. Step response of $G_\omega(s)$ under different r_b . (a) $r_b = [0.5 \ 0.75 \ 1]$; (b) $r_b = [1 \ 2 \ 5 \ 10]$; (c) $r_b = 0.2$; (d) $r_b = 0.14$.

4.4. Influence of r_b on Disturbance Rejection Performance

According to Equation (24), the transfer function of speed with respect to the unknown disturbance is described as:

$$G_f(s) = \frac{\omega_r(s)}{F_{1n}(s)} = \frac{r_b s G_1(s)}{R(s)} = \frac{r_b s (s^2 + (\beta_{1n} + k_n)s + (\beta_{1n} k_n + \beta_{2n}))}{r_b s^4 + (\beta_{1n} r_b + k_n r_b) s^3 + (\beta_{2n} r_b + \beta_{1n} k_n r_b) s^2 + (\beta_{2n} k_n + \beta_{3n}) s + \beta_{3n} k_n} \tag{33}$$

Figure 7 demonstrates the disturbance rejection performance of the LADRC-based drive system under different r_b . It can be noted that as long as the system is stable, i.e., $r_b \geq 0.2$, the disturbance rejection performance increases as r_b decreases. Moreover, under the same r_b , the disturbance rejection performance in the medium-frequency range is relatively weaker than that in the low- or high-frequency range.

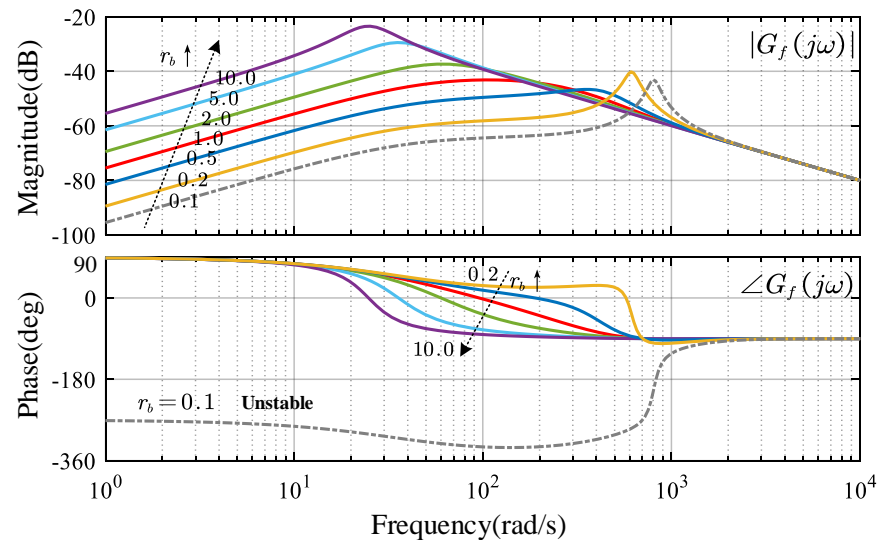


Figure 7. Bode diagram of $G_f(s)$ under different r_b .

Figure 8 shows the step response of the transfer function $G_f(s)$ under different r_b . It can be noted that as long as the system is stable, the external step unknown disturbance will be quickly rejected by the LADRC. The overshoot decreases as r_b decreases, which means that the disturbance rejection performance increases. These results are in accordance

with the above frequency analysis. Finally, it is concluded that the overestimation of inertia, i.e., $r_b < 1$, is beneficial for the disturbance rejection performance of the LADRC.

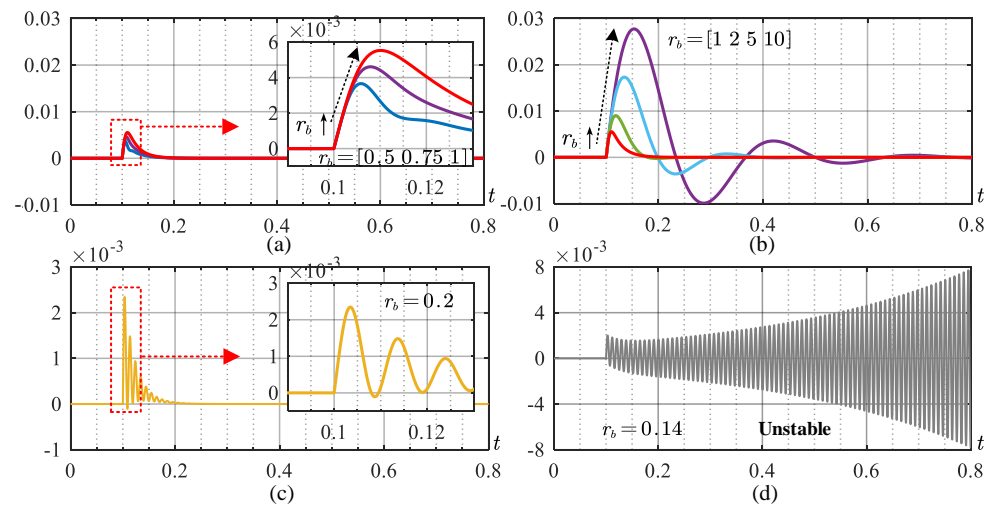


Figure 8. Step response of $G_f(s)$ under different r_b . (a) $r_b = [0.5 \ 0.75 \ 1]$; (b) $r_b = [1 \ 2 \ 5 \ 10]$; (c) $r_b = 0.2$; (d) $r_b = 0.14$.

According to the above analysis, it can be found that the inertia mismatch can significantly influence the performance of the LADRC-based drive system. Small r_b , i.e., overestimated inertia, can enhance the disturbance rejection performance to a certain degree, but may lead the system to be unstable. As for the tracking performance, it is found that the system will not achieve the desired response as long as $r_b \neq 1$. Therefore, to obtain a good tracking performance as well as guarantee the system’s stability, it is necessary to identify the load inertia.

5. Improved LADRC-Based Speed Regulator with Load Inertia Identification

Currently, various methods have been proposed for load inertia identification, such as the speed response-based method [27], the model reference adaptive system (MRAS) [28], the extended Kalman filter (EKF) [29,30], the orthogonal principle-based method [31,32], and the observer-based method [33]. Although these methods can be applied to the LADRC-based drive system, the additional identification unit will complicate the system, and increase the computational burden to the controller. In fact, the unknown disturbance estimated by the speed loop LESO already contains the inertia mismatch information. Therefore, it would be more efficient to identify the inertia by directly making use of the estimated unknown disturbance rather than introducing an additional identification unit. In this section, an inertia identification method based on the speed loop LESO is proposed. With the identified inertia, the modeled load inertia can be automatically adjusted, hence improving the overall performance of the LADRC-based drive system.

5.1. Design of the LESO-Based Inertia Identification Method

The mechanical motion equation is rewritten as follows by taking the inertia mismatch into consideration:

$$(J_0 + \tilde{J})\dot{\omega}_r = T_e - T_L - B\omega_r \tag{34}$$

where $J_0 + \tilde{J} = J$, J_0 is the initial value, and \tilde{J} is the error between the initial value and the actual value of inertia. Through defining $b_{n0} = 1/J_0$, Equation (4) is rewritten as:

$$\begin{cases} \dot{\theta}_r = \omega_r \\ \dot{\omega}_r = f_{0n} + f_{1n} + b_{n0}T_e^* \\ f_{0n} = b_{n0}(T_e - T_e^*) - b_{n0}B\dot{\omega}_r \\ f_{1n} = -b_{n0}T_L - b_{n0}B(\omega_r - \hat{\omega}_r) + n_n(t) - b_{n0}\tilde{J}\dot{\omega}_r \end{cases} \tag{35}$$

It can be seen in Equation (35) that the unknown disturbance f_{1n} contains the information of \tilde{J} . Therefore, it is possible to identify the inertia by making use of the estimated unknown disturbance obtained by the speed loop LESO.

In order to identify the inertia, the coefficient of \tilde{J} in Equation (35) should not be zero. Therefore, the IPMSM should be actuated in a speed-varying operation, i.e., $\dot{\omega}_r \neq 0$. A simple way to conduct the identification process is to force the IPMSM to operate at two different constant accelerations for a short period of time. Meanwhile, the external load torque T_L remains the same.

The speed reference of the LADRC-based drive system is shown in Figure 9. During the operation, the estimated unknown disturbances at the acceleration moment t_1 and deceleration moment t_2 are stored:

$$\begin{cases} z_{3n}(t_1) = -b_{n0}T_L(t_1) - b_{n0}B[\omega_r(t_1) - \hat{\omega}_r(t_1)] + n_n(t_1) - b_{n0}\tilde{J}\dot{\omega}_r(t_1) \\ z_{3n}(t_2) = -b_{n0}T_L(t_2) - b_{n0}B[\omega_r(t_2) - \hat{\omega}_r(t_2)] + n_n(t_2) - b_{n0}\tilde{J}\dot{\omega}_r(t_2) \end{cases} \quad (36)$$

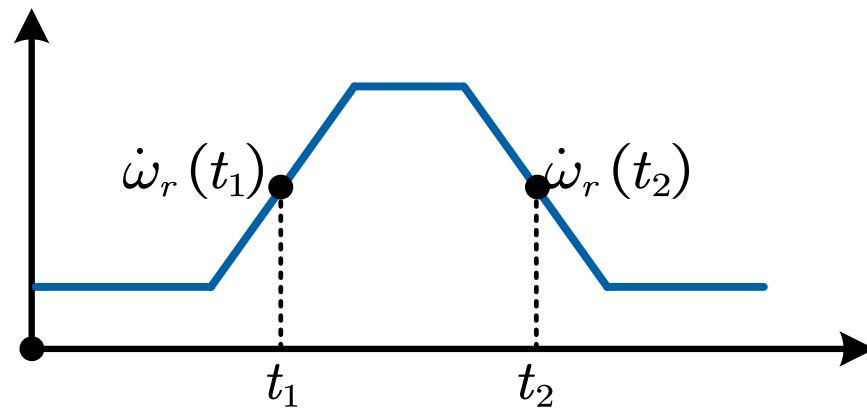


Figure 9. Required speed trajectory for inertia identification.

According to the analysis in Section 4.3, the tracking performance of the LADRC-based speed regulator has a good tolerance for inertia mismatch in low-frequency range. Therefore, the regulator can track the ramp speed reference in Figure 9 accurately, i.e., $\omega_r(t_1) = \hat{\omega}_r(t_1)$, and $\omega_r(t_2) = \hat{\omega}_r(t_2)$. Furthermore, the external load torque remains the same during the speed transition, i.e., $T_L(t_1) = T_L(t_2)$. Moreover, the difference between the unmodeled dynamics $n_n(t_1)$ and $n_n(t_2)$ can be neglected. Then, \tilde{J} is obtained as:

$$\tilde{J} = -\frac{z_{3n}(t_2) - z_{3n}(t_1)}{b_{n0}[\dot{\omega}_r(t_2) - \dot{\omega}_r(t_1)]} = -J_0 \frac{z_{3n}(t_2) - z_{3n}(t_1)}{\dot{\omega}_r(t_2) - \dot{\omega}_r(t_1)} \quad (37)$$

Finally, the identified inertia is expressed as:

$$\hat{J} = J_0 + \tilde{J} = J_0 \left[1 - \frac{z_{3n}(t_2) - z_{3n}(t_1)}{\dot{\omega}_r(t_2) - \dot{\omega}_r(t_1)} \right] \quad (38)$$

5.2. Improved LADRC-Based Speed Regulator

With the inertia identified, the estimated critical gain \hat{b}_n can be automatically adjusted, hence improving the overall performance of the LADRC-based drive system. The block diagram of the improved LADRC-based speed regulator is shown in Figure 10. In practical applications, the initial inertia J_0 is required. Since the accurate inertia will finally be identified by the proposed method, the initial inertia does not have to be set as accurately as possible. According to the analysis in Section 4.2, it is suggested that a large J_0 be chosen so as to guarantee the stability of the system.

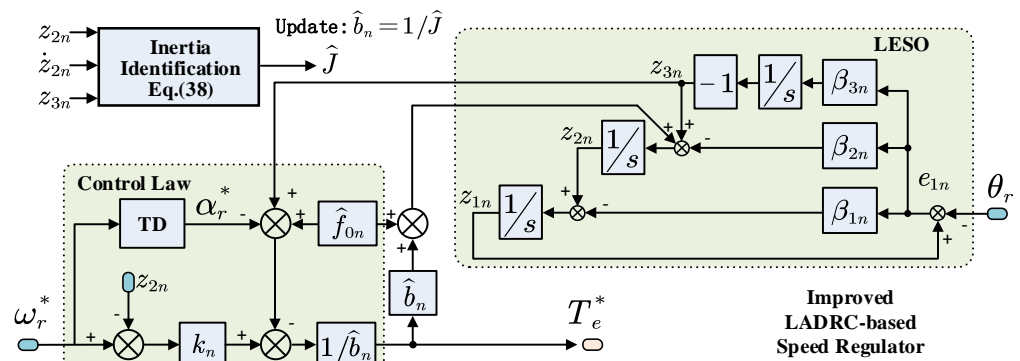


Figure 10. Block diagram of the improved LADRC-based speed regulator.

6. Experimental Results

In this section, experimental results of the proposed LADRC-based IPMSM drive system are presented. Figure 11 shows the experimental platform. The target machine under test is a three-phase IPMSM, the parameters of which are listed in Table 1. The IPMSM is driven by a two-level VSI. The control algorithm is implemented on a dSPACE MicroLabBox real-time platform. The dSPACE controller is connected to the VSI through a modulation board. The load torque is provided by an induction machine, which is mechanically coupled with the test machine and controlled by an AC driver. A photoelectric encoder with 2500 threads is utilized to acquire the actual rotor position. The experimental data is transmitted from dSPACE to a desktop computer in digital form through an 100 M ethernet cable. Then, the data is saved to a local directory by ControlDesk (dSPACE GmbH, Paderborn, Germany), the desktop software for dSPACE. Finally, the data is imported to OriginPro software and plotted.

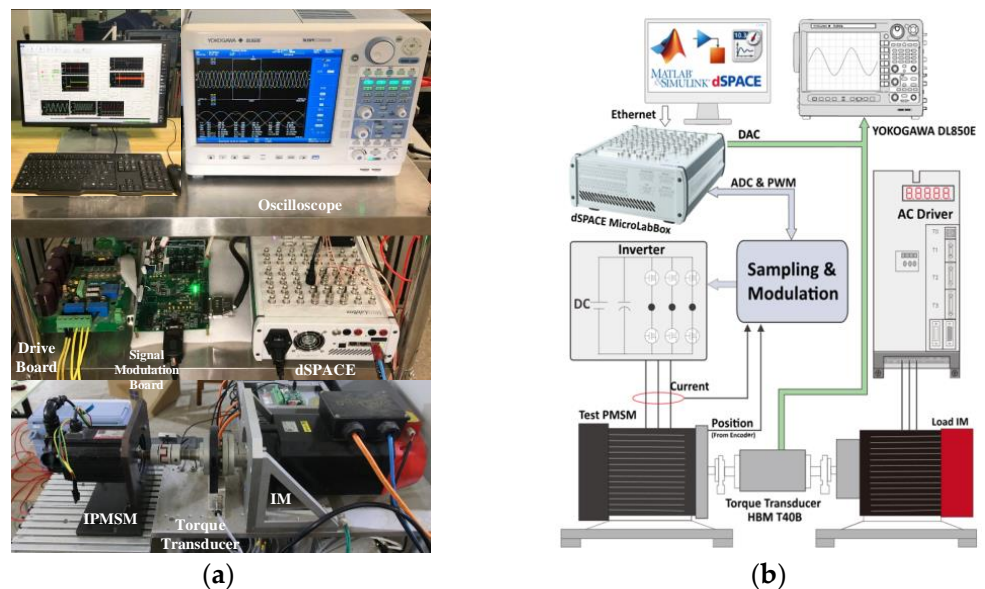
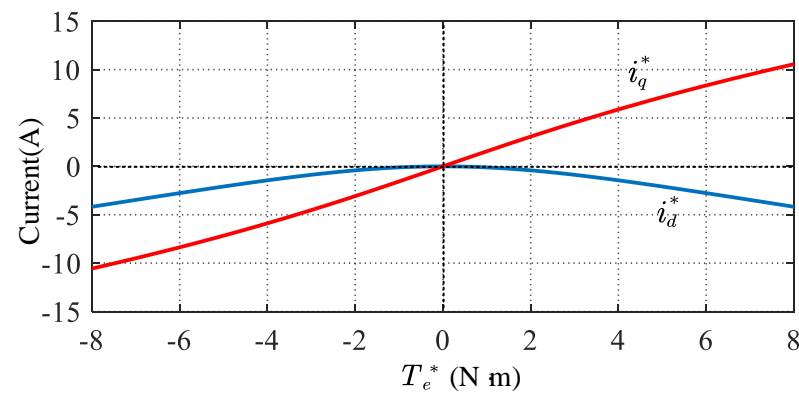


Figure 11. (a) Experimental platform. (b) Block diagram of the platform.

In the following experiments, the sampling and PWM switching frequency are both set to 5 kHz. The deadtime of PWM is set to 1 μs. The DC-link voltage is set to 240 V. The IPMSM is operated in MTPA mode. To reduce the computation burden, the MTPA scheme is implemented by means of look-up tables with offline calculations. The relationship between the torque reference and the *d-q*-axis current references under MPTA operation mode is shown in Figure 12.

Table 1. IPMSM Parameters.

| Parameters | Symbols | Values |
|------------------------------|------------|--------------------------|
| Rated Power | P_N | 1.0 kW |
| Rated Speed | ω_N | 1500 rpm |
| Rated Current | I_N | 8 A |
| Number of Pole Pairs | n_p | 3 |
| Rotor Flux Linkage | ψ_f | 0.142 V·s |
| Stator Resistance | R_s | 0.75 Ω |
| d -axis Inductance | L_d | 3.5 mH |
| q -axis Inductance | L_q | 9.8 mH |
| Load Inertia | J | 0.0174 kg·m ² |
| Viscous Friction Coefficient | B | 0.00075 N·m·s/rad |

**Figure 12.** Relationship between T_e^* and i_d^* , i_q^* under MPTA operation mode.

It should be noted that this article mainly concentrates on researching the speed control performance of the LADRC-based drive system. Hence, during the experiments, the parameters for the current loop LADRC are fixed to $k_d = k_q = 200\pi$, $\omega_{0i} = 1200\pi$. Furthermore, considering the driving capability of the power converter, the torque limit for the speed loop output is set to $T_{e\max}^* = 6 \text{ N}\cdot\text{m}$.

6.1. Experimental Results of the LADRC-Based IPMSM Drive System with Accurate Inertia

In this experiment, the tracking performance and the disturbance rejection performance of the LADRC-based IPMSM drive system with accurate inertia are evaluated.

Figure 13 shows the experimental results of the speed response with step speed reference from 0 rpm to 1500 rpm. From top to bottom, the plotted signals are ω_r , i_q , and i_d . In Figure 13a, three groups of experiment results with the same ω_{0n} and different k_n are presented and compared, where $\omega_{0n} = 80\pi$, $k_n = [5\pi, 10\pi, 20\pi]$. In Figure 13b, three groups of experiment results with the same k_n and different ω_{0n} are presented and compared, where $k_n = 10\pi$, $\omega_{0n} = [40\pi, 80\pi, 120\pi]$. It can be seen that the speed tracking performance is mainly dependent on k_n . A larger k_n brings a faster response. It should be noted that since there is a limitation for the speed loop output, the maximum acceleration of speed is restricted. Therefore, the speed response with the step speed reference is actually a ramp response rather than a step response.

Figure 14 shows the experimental results of the speed response with sinusoidal speed reference. The offset, the amplitude, and the frequency of the sinusoidal reference are 1500 rpm, 20 rpm, and 15 Hz, respectively, i.e., $\omega_r^* = 1500 + 20 \sin 30\pi \text{ rpm}$. From top to bottom, the plotted signals are ω_r , i_q , i_d , e_{1n} , and z_{3n} . In Figure 14a, three groups of experiment results with the same ω_{0n} and different k_n are presented and compared, where $\omega_{0n} = 160\pi$, $k_n = [40\pi, 80\pi, 120\pi]$. In Figure 14b, three groups of experiment results with the same k_n and different ω_{0n} are presented and compared, where $k_n = 80\pi$, $\omega_{0n} = [80\pi, 120\pi, 160\pi]$.

Obviously, the speed tracking performance is mainly dependent on k_n . A larger k_n brings a lower tracking latency and a smaller amplitude attenuation.

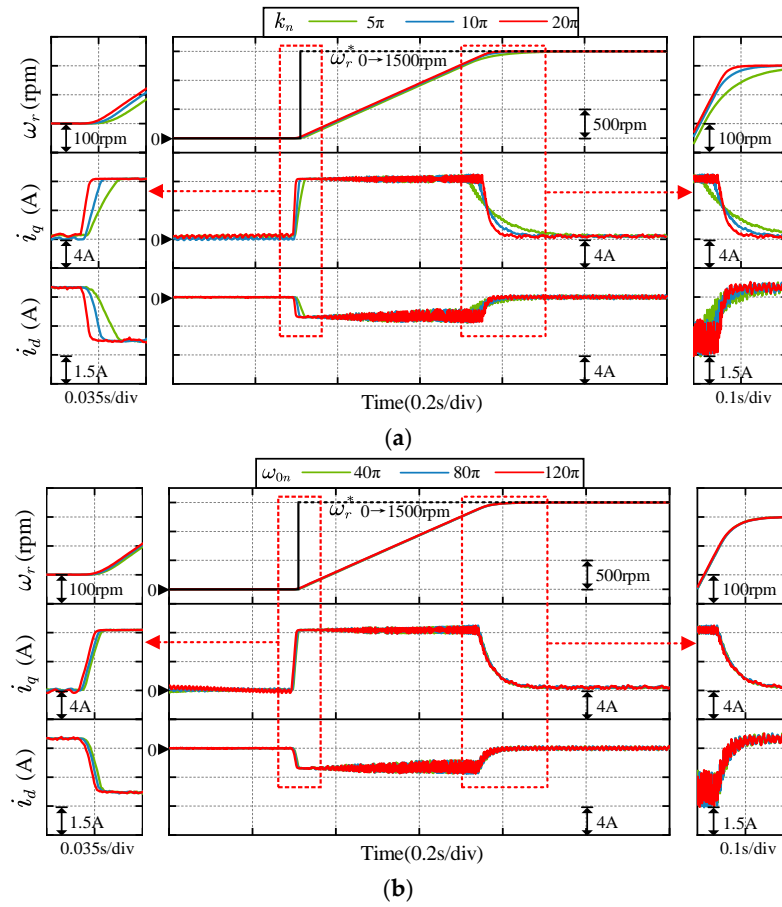


Figure 13. Experimental results of the speed response with step speed reference from 0 rpm to 1500 rpm. (a) Under different k_n , where $\omega_{0n} = 80\pi$, $k_n = [5\pi, 10\pi, 20\pi]$; (b) under different ω_{0n} , where $k_n = 10\pi$, $\omega_{0n} = [40\pi, 80\pi, 120\pi]$.

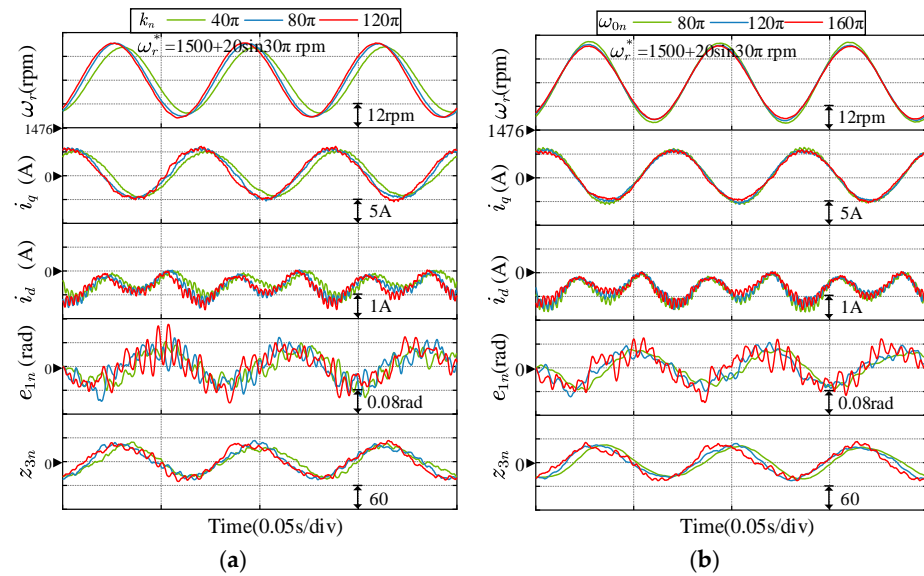


Figure 14. Experimental results of the speed response with sinusoidal speed reference. (a) Under different k_n , where $\omega_{0n} = 160\pi$, $k_n = [40\pi, 80\pi, 120\pi]$; (b) under different ω_{0n} , where $k_n = 80\pi$, $\omega_{0n} = [80\pi, 120\pi, 160\pi]$.

Figure 15 shows the experimental results of the speed response with step load disturbance. The test IPMSM operates at 1500 rpm. The load IM provides an external step load torque of 3 N·m at 0.3 s. From top to bottom, the plotted signals are ω_r , i_q , i_d , e_{1n} , and z_{3n} . In Figure 15a, three groups of experiment results with the same ω_{0n} and different k_n are presented and compared, where $\omega_{0n} = 80\pi$, $k_n = [5\pi, 10\pi, 20\pi]$. In Figure 15b, three groups of experiment results with the same k_n and different ω_{0n} are presented and compared, where $k_n = 10\pi$, $\omega_{0n} = [40\pi, 80\pi, 120\pi]$. It can be seen that a larger k_n or a larger ω_{0n} are both helpful for improving the disturbance rejection performance, and the improvement is relatively more significant when increasing ω_{0n} .

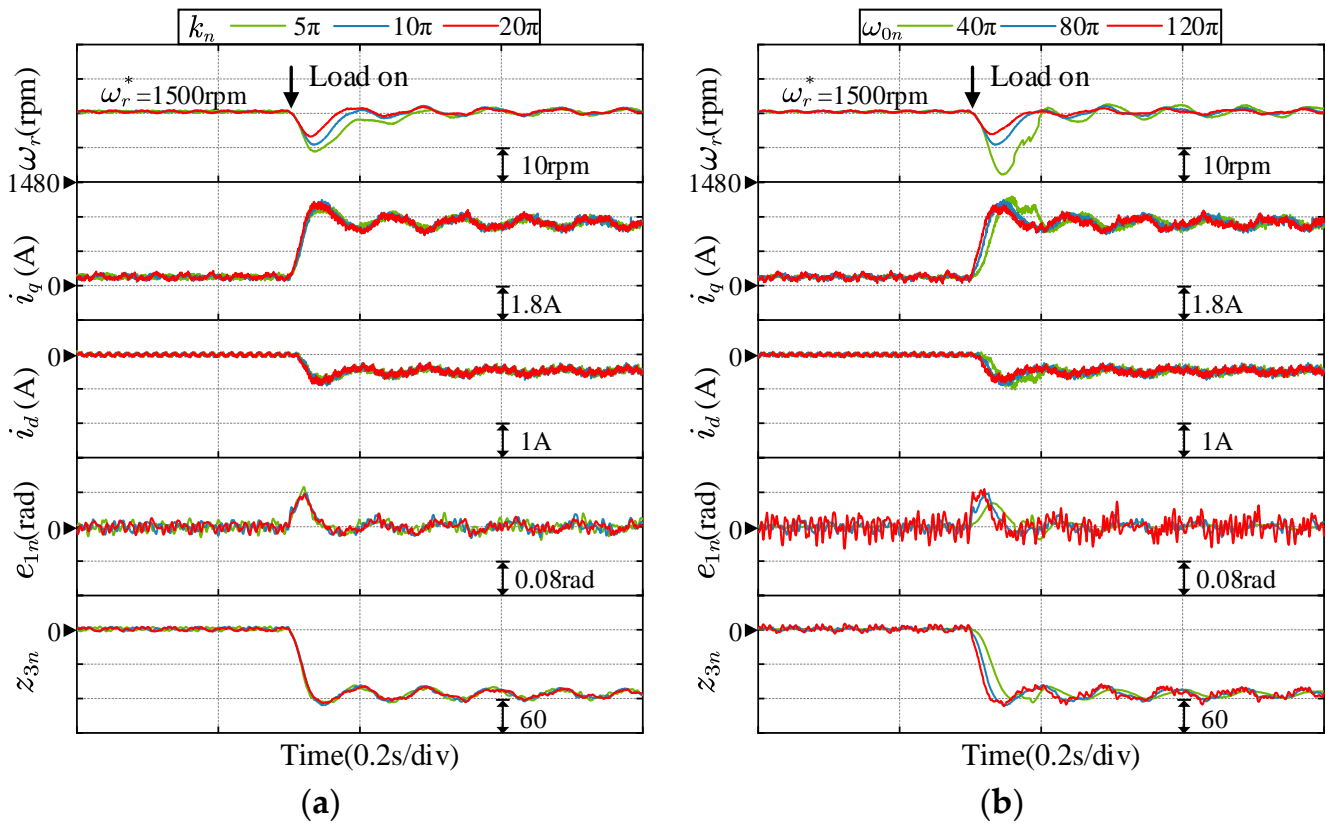


Figure 15. Experimental results of the speed response with step load disturbance. (a) Under different k_n , where $\omega_{0n} = 80\pi$, $k_n = [5\pi, 10\pi, 20\pi]$; (b) under different ω_{0n} , where $k_n = 10\pi$, $\omega_{0n} = [40\pi, 80\pi, 120\pi]$.

6.2. Experimental Results of the LADRC-Based IPMSM Drive System with Mismatched Inertia

In the following experiment, the tracking performance and the disturbance rejection performance of the LADRC-based IPMSM drive system with mismatched inertia are evaluated.

Figure 16 shows the experimental results of the speed response with step speed reference. Three groups of experiment results with different r_b are presented and compared, where $\omega_{0n} = 120\pi$, $k_n = 10\pi$, $r_b = [0.5, 1, 2]$. It can be seen that the speed responses in the three experiments are almost the same. This can be explained according to the analysis in Figure 5. Since there is a limitation for the speed loop output, the maximum acceleration of speed is restricted. Therefore, the speed response with the step speed reference is actually a ramp response. The ramp speed lies in the low-frequency range in Figure 5. Therefore, the inertia mismatch has little effect on the speed tracking performance.

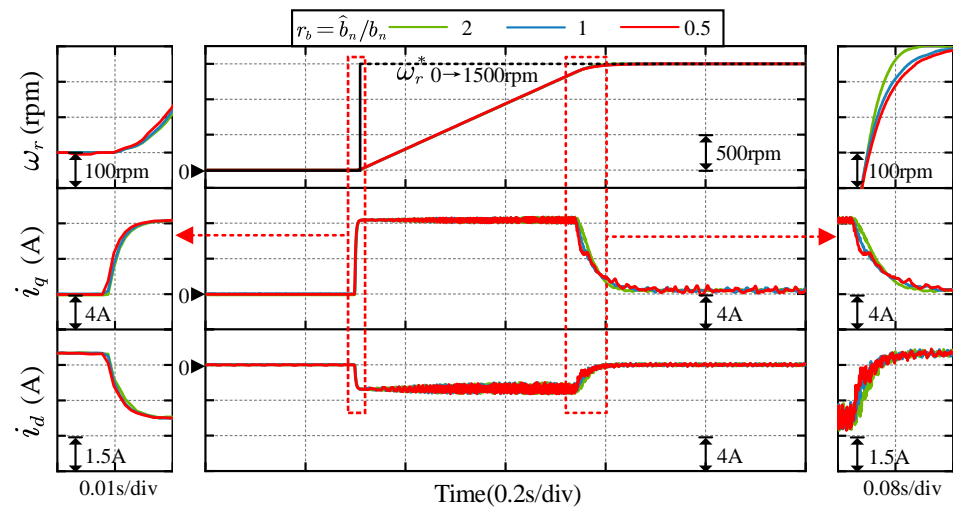


Figure 16. Experimental results of the speed response with step speed reference from 0 rpm to 1500 rpm under different r_b , where $\omega_{0n} = 120\pi$, $k_n = 10\pi$, $r_b = [0.5, 1, 2]$.

Figure 17 shows the experimental results of the speed response with sinusoidal speed reference. Three groups of experiment results with different r_b are presented and compared, where $\omega_{0n} = 120\pi$, $k_n = 80\pi$, $r_b = [0.5, 1, 2]$. It can be seen that $r_b = 2$ leads to amplitude amplification and phase delay, while $r_b = 0.5$ leads to amplitude attenuation and phase advance. This is because the 15 Hz sinusoidal reference lies in the middle-frequency range in Figure 5. As for the high-frequency range, the corresponding experiments are unable to conduct due to the current limitation of the power converter.

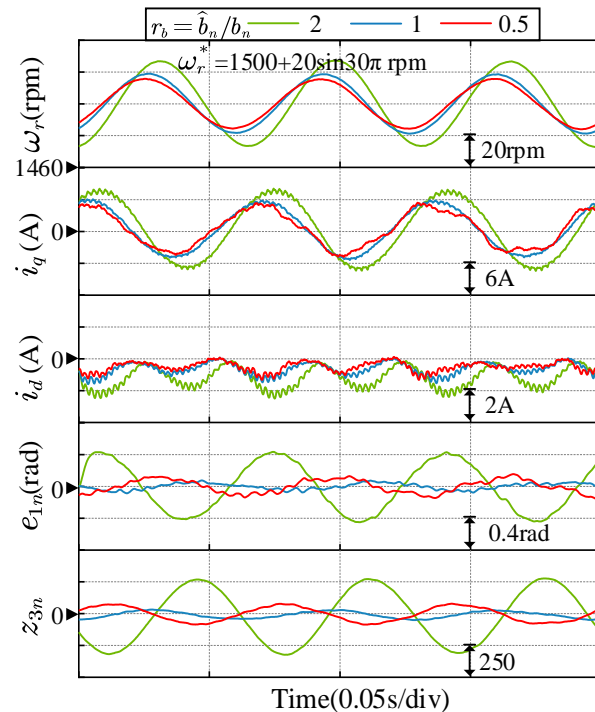


Figure 17. Experimental results of the speed response with sinusoidal speed reference under different r_b , where $\omega_{0n} = 120\pi$, $k_n = 80\pi$, $r_b = [0.5, 1, 2]$.

Figure 18 shows the experimental results of the speed response with step load disturbance. Three groups of experiment results with different r_b are presented and compared, where $\omega_{0n} = 120\pi$, $k_n = 10\pi$, $r_b = [0.5, 1, 2]$. It can be seen that the speed fluctuation

during the loading/unloading process decreases as r_b decreases, which indicates that the system's disturbance rejection performance increases as r_b decreases. These results accord with the analysis in Figure 6.

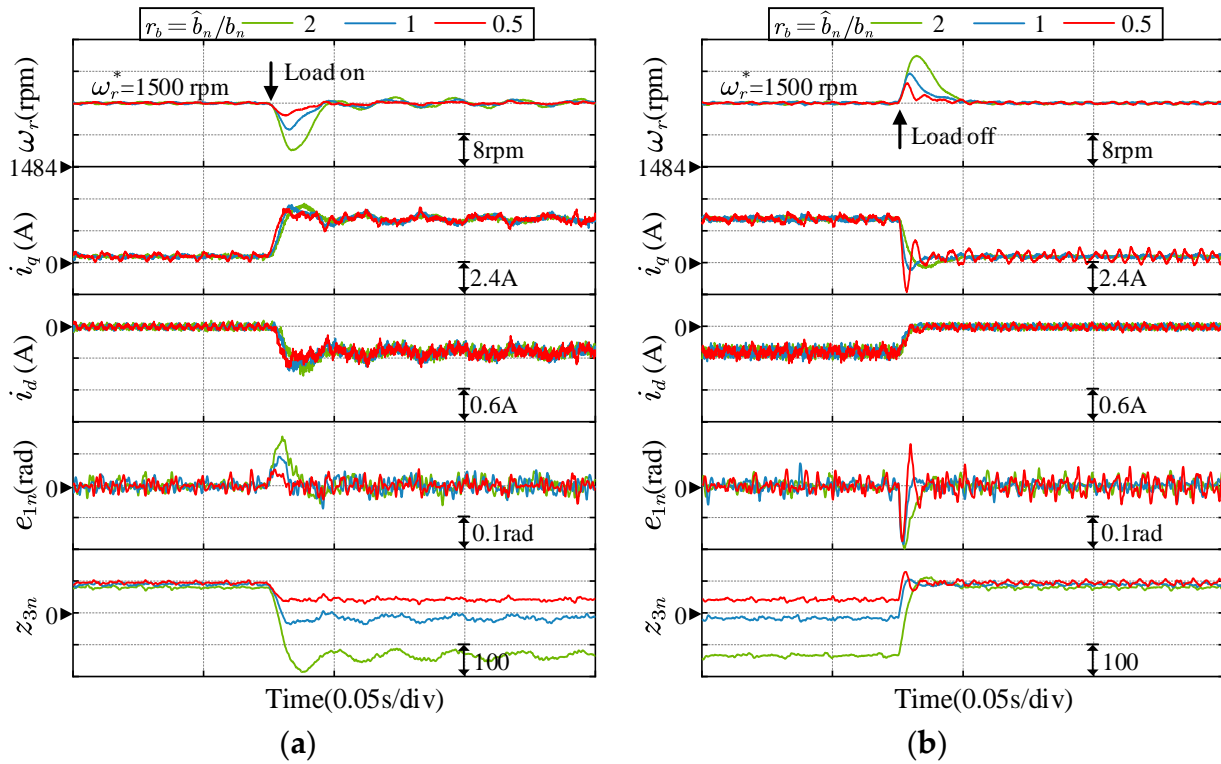


Figure 18. Experimental results of the speed response with step load disturbance under different r_b , where $\omega_{0n} = 120\pi$, $k_n = 10\pi$, $r_b = [0.5, 1, 2]$. (a) Loading; (b) unloading.

6.3. Experimental Results of the Proposed Inertia Identification Method

During this experiment, the IPMSM makes a speed transition from 300 rpm to 1000 rpm, and then back to 300 rpm. The controller parameters are set to $\omega_{0n} = 120\pi$, $k_n = 10\pi$. Figure 19a,b shows the experimental results with initial inertia respectively set to $0.5J$ and $2J$. It can be seen that the identified inertia converges quickly within 0.3 s, and the identified value is close to the actual value, which is $0.0174 \text{ kg}\cdot\text{m}^2$.

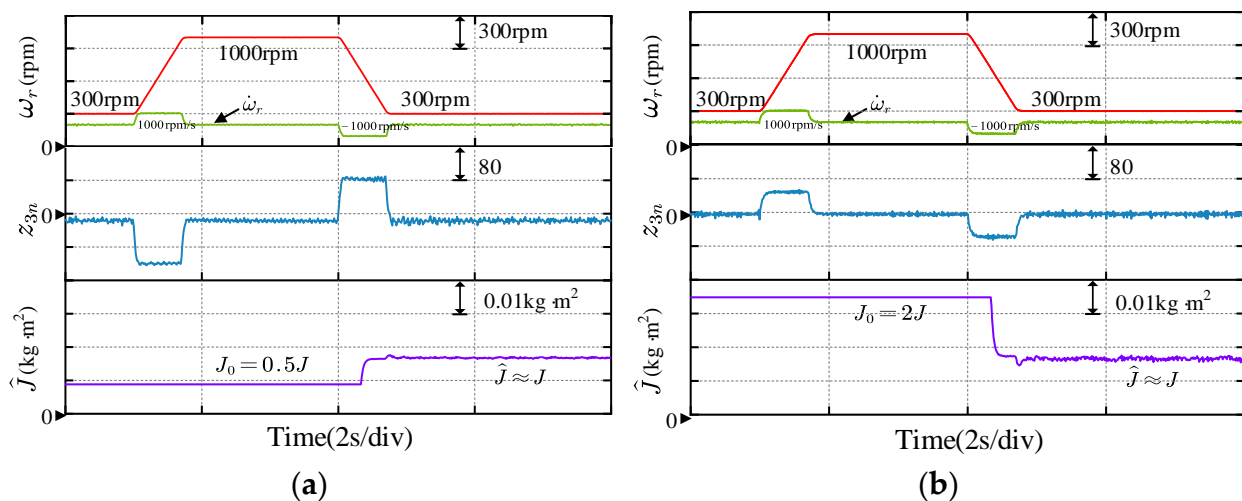


Figure 19. Experimental results of the proposed inertia identification method under different initial inertia. (a) $J_0 = 0.5J$; (b) $J_0 = 2J$.

7. Conclusions

In this article, an improved LADRC scheme for an IPMSM drive system is proposed. The proposed LADRC for speed regulation adopts position feedback instead of speed feedback so that the low-pass filter can be eliminated. Moreover, the MTPA scheme is incorporated into the proposed LADRC to improve the IPMSM drive performance by making full use of its reluctance torque. In addition, considering that the load inertia may vary in some applications, the stability, the tracking performance, and the disturbance rejection performance of the LADRC-based control system with mismatched inertia are analyzed in detail. It is found that the overestimation of inertia can enhance the disturbance rejection performance, but may lead the system to be unstable. As for the tracking performance, it is found that the system will not achieve the desired response as long as the inertia is mismatched. Then, to pursue a good tracking performance as well as guarantee the system's stability, an inertia identification method is proposed, which extracts the mismatch information from the estimated disturbance. Extensive experimental results validate the correctness of the theoretical analysis and the effectiveness of the proposed scheme.

However, the designed controller in this article is based on an ideal IPMSM model, where the iron losses, the non-sinusoidal back-EMF, the cross-coupling, and the core saturation effect are not considered. In real applications, these unmodelled parts will bring additional disturbance to the drive system and increase the estimation burden of LESO. Thus, the overall performance of the LADRC-based drive system will be degraded. In further research, a more accurate model of IPMSM should be adopted.

Author Contributions: Conceptualization, F.J.; Formal analysis, S.S.; Funding acquisition, K.Y.; Project administration, K.Y.; Software, F.Y.; Supervision, K.Y.; Writing—original draft, F.J.; Writing—review & editing, F.J. All authors have read and agreed to the published version of the manuscript.

Funding: This work was supported by The National Key R & D Program of China (Grant No.2018YFB0904800), The National Natural Science Foundation of China (Grant No.51677078), and The Science Technology and Innovation Commission of Shenzhen Municipality (Grant No. JCYJ20170307160832442).

Conflicts of Interest: The authors declare no conflict of interest.

Appendix A

The goal of MTPA scheme is to achieve the desired torque with minimum stator current required. Such a scheme can be described as:

$$\begin{cases} T_e = \frac{3}{2}n_p [\psi_f + (L_d - L_q)i_d]i_q \\ i_s = \min(\sqrt{i_d^2 + i_q^2}) \end{cases} \quad (A1)$$

To solve the problem described in Equation (A1), the Lagrange multiplier method can be adopted. This method is commonly used for obtaining the maximum/minimum value of a function with specific constraints. The Lagrange auxiliary function for Equation (A1) is constructed as:

$$L(i_d, i_q, \lambda) = \sqrt{i_d^2 + i_q^2} + \lambda \cdot \left\{ T_e - \frac{3}{2}n_p [\psi_f + (L_d - L_q)i_d]i_q \right\} \quad (A2)$$

where λ is the Lagrange multiplier. Let the partial derivatives of L with respect to i_d , be i_q , and λ is equal to zero:

$$\frac{\partial L}{\partial i_d} = \frac{i_d}{\sqrt{i_d^2 + i_q^2}} - \frac{3}{2}\lambda n_p (L_d - L_q)i_q = 0 \quad (A3)$$

$$\frac{\partial L}{\partial i_q} = \frac{i_q}{\sqrt{i_d^2 + i_q^2}} - \frac{3}{2}\lambda n_p [\psi_f + (L_d - L_q)i_d] = 0 \quad (A4)$$

$$\frac{\partial L}{\partial \lambda} = T_e - \frac{3}{2}n_p [\psi_f + (L_d - L_q)i_d]i_q = 0 \quad (\text{A5})$$

Combining Equations (A3) and (A4), the relationship between i_d and i_q under MTPA operation can be derived:

$$i_q = \sqrt{\frac{\psi_f i_d}{L_d - L_q} + i_d^2} \quad (\text{A6})$$

Substituting Equation (A6) into Equation (A5), the relationship between T_e and i_d is derived:

$$T_e = \frac{3}{2}n_p [\psi_f + (L_d - L_q)i_d] \sqrt{\frac{\psi_f i_d}{L_d - L_q} + i_d^2} \quad (\text{A7})$$

On the other hand, the inverse function of Equation (A6) is derived as:

$$i_d = \frac{-\psi_f + \sqrt{\psi_f^2 + 4i_q^2(L_d - L_q)^2}}{2(L_d - L_q)} \quad (\text{A8})$$

Substituting Equation (A8) into Equation (A5), the relationship between T_e and i_q is derived:

$$T_e = \frac{3}{4}n_p \left[\psi_f + \sqrt{\psi_f^2 + 4i_q^2(L_d - L_q)^2} \right] i_q \quad (\text{A9})$$

References

1. Lin, F.J.; Hung, Y.C.; Chen, J.M. Sensorless IPMSM drive system using saliency back-EMF-based intelligent torque observer with MTPA control. *IEEE Trans. Ind. Inform.* **2014**, *10*, 1226–1241.
2. Hernandez-Guzman, V.M.; Silva-Ortigoza, R. PI control plus electric current loops for PM synchronous motors. *IEEE Trans. Control Syst. Technol.* **2010**, *19*, 868–873. [[CrossRef](#)]
3. GrCar, B.; Cafuta, P.; Znidaric, M. Nonlinear control of synchronous servo drive. *IEEE Trans. Control Syst. Technol.* **1996**, *4*, 177–184. [[CrossRef](#)]
4. Vu, N.T.T.; Yu, D.Y.; Choi, H.H. T-S fuzzy-model-based sliding-mode control for surface-mounted permanent-magnet synchronous motors considering uncertainties. *IEEE Trans. Ind. Electron.* **2012**, *60*, 4281–4291. [[CrossRef](#)]
5. Mohd, Z.F.; Mekhilef, S.; Mubin, M. Robust speed control of PMSM using sliding mode control (SMC)—A review. *Energies* **2019**, *12*, 1669. [[CrossRef](#)]
6. Gao, J.; Gong, C.; Li, W. Novel compensation strategy for calculation delay of finite control set model predictive current control in PMSM. *IEEE Trans. Ind. Electron.* **2019**, *67*, 5816–5819. [[CrossRef](#)]
7. Ei-Sousy, F.F.M. Hybrid H ∞ -based wavelet neural network tracking control for permanent magnet synchronous motor servo drive. *IEEE Trans. Ind. Electron.* **2010**, *57*, 3157–3166. [[CrossRef](#)]
8. Wang, W.; Tan, F.; Wu, J. Adaptive integral backstepping controller for PMSM with AWPSO parameters optimization. *Energies* **2019**, *12*, 2596. [[CrossRef](#)]
9. Lin, F.J.; Chen, S.Y.; Lin, W.T. An Online Parameter Estimation Using Current Injection with Intelligent Current-Loop Control for IPMSM Drives. *Energies* **2021**, *14*, 8138. [[CrossRef](#)]
10. Mendoza-Mondragón, F.; Hernández-Guzmán, V.M.; Rodríguez-Reséndiz, J. Robust speed control of permanent magnet synchronous motors using two-degrees-of-freedom control. *IEEE Trans. Ind. Electron.* **2018**, *65*, 6099–6108. [[CrossRef](#)]
11. Guo, B.; Bacha, S.; Alamir, M. A review on ADRC based PMSM control designs. In Proceedings of the 2017 IEEE 43rd Annual Conference of the IEEE Industrial Electronics Society, Beijing, China, 29 October–1 November 2017; pp. 1747–1753.
12. Han, J. From PID to active disturbance rejection control. *IEEE Trans. Ind. Electron.* **2009**, *56*, 900–906. [[CrossRef](#)]
13. Gao, Z. Scaling and bandwidth-parameterization based controller tuning. In Proceedings of the American Control Conference, Denver, CO, USA, 4–6 June 2003; pp. 4989–4996.
14. Du, B.; Wu, S.; Han, S. Application of linear active disturbance rejection controller for sensorless control of internal permanent-magnet synchronous motor. *IEEE Trans. Ind. Electron.* **2016**, *63*, 3019–3027. [[CrossRef](#)]
15. Zhou, K.; Ai, M.; Sun, Y. PMSM vector control strategy based on active disturbance rejection controller. *Energies* **2019**, *12*, 3827. [[CrossRef](#)]
16. Liu, C.; Luo, G.; Duan, X. Adaptive LADRC-based disturbance rejection method for electromechanical servo system. *IEEE Trans. Ind. Appl.* **2019**, *56*, 876–889. [[CrossRef](#)]
17. Wang, G.; Liu, R.; Zhao, N. Enhanced linear ADRC strategy for HF pulse voltage signal injection-based sensorless IPMSM drives. *IEEE Trans. Power Electron.* **2018**, *34*, 514–525. [[CrossRef](#)]

18. Zuo, Y.; Zhu, X.; Quan, L. Active disturbance rejection controller for speed control of electrical drives using phase-locking loop observer. *IEEE Trans. Ind. Electron.* **2018**, *66*, 1748–1759. [[CrossRef](#)]
19. Yin, Z.; Du, C.; Liu, J. Research on autodisturbance-rejection control of induction motors based on an ant colony optimization algorithm. *IEEE Trans. Ind. Electron.* **2017**, *65*, 3077–3094. [[CrossRef](#)]
20. Kumar, P.; Beig, A.R.; Bhaskar, D.V.; Jaafari, K.A.; Muduli, U.R.; Behera, R.K. An Enhanced Linear Active Disturbance Rejection Controller for High Performance PMBLDCM Drive Considering Iron Loss. *IEEE Trans. Power Electron.* **2021**, *36*, 14087–14097. [[CrossRef](#)]
21. Hao, Z.; Yang, Y.; Gong, Y. Linear/Nonlinear Active Disturbance Rejection Switching Control for Permanent Magnet Synchronous Motors. *IEEE Trans. Power Electron.* **2021**, *36*, 9334–9347. [[CrossRef](#)]
22. Jin, H.; Song, J.; Lan, W. On the characteristics of ADRC: A PID interpretation. *Sci. China Inform. Sci.* **2020**, *63*, 1–3. [[CrossRef](#)]
23. Lin, P.; Wu, Z.; Fei, Z. A Generalized PID Interpretation for High-order LADRC and Cascade LADRC for Servo Systems. *IEEE Trans. Ind. Electron.* **2021**, *1*, 1–8. [[CrossRef](#)]
24. Jahns, T.M.; Kliman, G.B.; Neumann, T.W. Interior permanent-magnet synchronous motors for adjustable-speed drives. *IEEE Trans. Ind. Appl.* **1986**, *22*, 738–747. [[CrossRef](#)]
25. Uddin, M.N.; Radwan, T.S.; Rahman, M.A. Performance of interior permanent magnet motor drive over wide speed range. *IEEE Trans. Energy Convers.* **2002**, *17*, 79–84. [[CrossRef](#)]
26. Kim, Y.S.; Sul, S.K. Torque control strategy of an IPMSM considering the flux variation of the permanent magnet. In Proceedings of the 2007 IEEE Industry Applications Annual Meeting, New Orleans, LA, USA, 23–27 September 2007; pp. 1301–1307.
27. Kwon, T.S.; Sul, S.K.; Nakamura, H. Identification of the mechanical parameters for servo drive. In Proceedings of the Conference Record of the 2006 IEEE Industry Applications Conference Forty-First IAS Annual Meeting, Tampa, FL, USA, 8–12 October 2006; pp. 905–910.
28. Guo, Y.; Huang, L.; Muramatsu, M. Research on inertia identification and auto-tuning of speed controller for AC servo system. In Proceedings of the Power Conversion Conference, Osaka, Japan, 2–5 April 2002; pp. 896–901.
29. Szabat, K.; Orłowska-Kowalska, T. Application of the Kalman filters to the high-performance drive system with elastic coupling. *IEEE Trans. Ind. Electron.* **2012**, *59*, 4226–4235. [[CrossRef](#)]
30. Del, G.D.; Grillo, S. Analysis of the sensitivity of extended kalman filter-based inertia estimation method to the assumed time of disturbance. *Energies* **2019**, *12*, 483.
31. Awaya, I.; Kato, Y.; Miyake, I. New motion control with inertia identification function using disturbance observer. In Proceedings of the 1992 International Conference on Industrial Electronics, Control, Instrumentation and Automation, San Diego, CA, USA, 9–13 November 1992; pp. 77–81.
32. Li, S.; Liu, Z. Adaptive speed control for permanent-magnet synchronous motor system with variations of load inertia. *IEEE Trans. Ind. Electron.* **2009**, *56*, 3050–3059.
33. Feng, Y.; Yu, X.; Han, F. High-order terminal sliding-mode observer for parameter estimation of a permanent-magnet synchronous motor. *IEEE Trans. Ind. Electron.* **2012**, *60*, 4272–4280. [[CrossRef](#)]